



Cite as

Nano-Micro Lett.
(2024) 16:136Received: 4 October 2023
Accepted: 12 January 2024
© The Author(s) 2024

Building Feedback-Regulation System Through Atomic Design for Highly Active SO₂ Sensing

Xin Jia¹, Panzhe Qiao², Xiaowu Wang¹, Muyu Yan³, Yang Chen⁴, Bao-Li An¹, Pengfei Hu⁵, Bo Lu⁵, Jing Xu⁵, Zhenggang Xue¹ ✉, Jiaqiang Xu¹ ✉

HIGHLIGHTS

- Feedback-regulation system is established between single Pt sites and MoS₂ supports
- The Pt₁-MoS₂-def can expand the electron transfer path from single Pt sites to whole Pt-MoS₂ supports in SO₂ gas atmosphere.
- The Pt₁-MoS₂-def sensors exhibit high SO₂ responses and extremely low limit of detection (3.14% to 500 ppb SO₂) at room temperature.
- The Pt₁-MoS₂-def sensors array can realize real-time monitoring of SO₂ for plant growth.

ABSTRACT Reasonably constructing an atomic interface is pronouncedly essential for surface-related gas-sensing reaction. Herein, we present an ingenious feedback-regulation system by changing the interactional mode between single Pt atoms and adjacent S species for high-efficiency SO₂ sensing. We found that the single Pt sites on the MoS₂ surface can induce easier volatilization of adjacent S species to activate the whole inert S plane. Reversely, the activated S species can provide a feedback role in tailoring the antibonding-orbital electronic occupancy state of Pt atoms, thus creating a combined system involving S vacancy-assisted single Pt sites (Pt-Vs) to synergistically improve the adsorption ability of SO₂ gas molecules. Furthermore, in situ Raman, ex situ X-ray photoelectron spectroscopy testing and density functional theory analysis demonstrate the intact feedback-regulation system can expand the electron transfer path from single Pt sites to whole Pt-MoS₂ supports in SO₂ gas atmosphere. Equipped with wireless-sensing modules, the final Pt₁-MoS₂-def sensors array can further realize real-time monitoring of SO₂ levels and cloud-data storage for plant growth. Such a fundamental understanding of the intrinsic link between atomic interface and sensing mechanism is thus expected to broaden the rational design of highly effective gas sensors.



KEYWORDS Feedback-regulation system; Atomic interface; SO₂ sensor; Single-atom sensing mechanism; Intelligent-sensing array

Xin Jia and Panzhe Qiao have contributed equally to this work.

✉ Zhenggang Xue, zgxue@shu.edu.cn; Jiaqiang Xu, xujiaqiang@shu.edu.cn

¹ NEST Lab, Department of Chemistry, College of Sciences, Shanghai University, Shanghai 200444, People's Republic of China

² Shanghai Synchrotron Radiation Facility, Zhangjiang Lab, Shanghai Advanced Research Institute, Chinese Academy of Sciences, Shanghai 201204, People's Republic of China

³ School of Chemistry and Materials Science, University of Science and Technology of China, Hefei 230026, People's Republic of China

⁴ Key Laboratory of Organic Compound Pollution Control Engineering (MOE), School of Environmental and Chemical Engineering, Shanghai University, Shanghai 200444, People's Republic of China

⁵ Shanghai University, Instrumental Analysis & Research Center of Shanghai University, Shanghai 200444, People's Republic of China

Published online: 27 February 2024



SHANGHAI JIAO TONG UNIVERSITY PRESS

Springer

1 Introduction

Sulfur dioxide (SO_2) constitutes a significant proportion of harmful air pollutants, and the main sources of SO_2 gas include the combustion of sulfur-containing fuels in the manufacturing and construction sectors and volcanic eruptions and forest fires [1, 2]. Additionally, sulfur dioxide not only contributes to acid rain but also has detrimental effects on both human and plant growth [3]. Research has found that the sensitivity to SO_2 gas varies significantly among different plants, sensitive plants exposed to an atmosphere with 0.5 ppm of SO_2 exhibit chloroplast damage and photosynthesis stagnation after 8 h. When exposed to an atmosphere with 1–4 ppm of SO_2 , damage occurs within 3 h [4].

Sulfur dioxide gas sensors are widely applied in many fields, such as comprehensive treatment of environmental pollution [5], monitoring the quality of the healthy environment inspection [6, 7] and improving plant productivity [8]. Conventionally, SO_2 concentrations are measured using two optical tracking technologies, infrared radiation spectroscopy or UV absorbance spectroscopy. In the quest to achieve continuous monitoring of harmful pollution, solid-state resistive gas sensors employing semiconducting have been the widest spread in gas-sensing application owing to their compactness and versatility. In particular, the room temperature SO_2 sensors based on two-dimensional materials have gradually evolved into the development trend on account of their low power consumption (compared to required high working temperature for most oxide–semiconductor sensors) and small sizes (no integrated limitation for microheater and sensing layer) [9–11]. Given lacking supplied energy at high operation temperature to activate the sensing-layer, the performances of room-temperature SO_2 sensors are more dependent on the intrinsic activity of sensing materials. Compared with metal oxides semiconductor (MOS) sensors that work at high temperatures, molybdenum disulfide has been extensively studied for its excellent gas-sensing property at the room temperature. For example, previous study has demonstrated that doping transition metal to inner MoS_2 supports can markedly improve the SO_2 sensing property [12]. Therefore, engineering highly active sensitive materials to meet the requirements of high sensitivity and low limit of detection (LOD) for room-temperature SO_2 detection is crucial, yet challenging.

In recent years, single-atom catalysts (SACs) have been considered as potential candidates for high-performance

gas sensors due to their maximum utilization efficiency of metal atoms and uniform unsaturated configuration of active centers [13–17]. Generally, the single metal centers (especially for Pd, Pt, Au and so on) are considered as highly active adsorption and reactive sites during the gas-sensing process [18–22]. The sensitization action mainly involves chemical and electronic effects. On the one hand, the unsaturated metal center can reinforce the bonding process to objective gas molecules and lead potential activation of gas molecules [23, 24]. On the other hand, the metal center can also induce more electron transfer with the target gas molecules to improve the sensing response [25]. However, this sensitization action may result in a major electron concentration localized at these single-metal sites [13, 16, 26, 27], while the participation of support materials is often ignored. Considering the extremely low single metal loadings, activating the main support materials are thus considered as a crucial strategy to further enhance the gas-sensing performance. Meanwhile, the interactive status between single-atom centers and the whole activated supports may trigger the linkage effect to synergistically enhance the gas adsorption and electronic transform process. This route of reaction mechanism is thus apparently different from that of traditional SACs. However, engineering active support-associated SACs and deeply exploring the gas-sensing action are still rarely studies.

Here, we present an ingenious feedback-regulation system by changing the interactional mode between single Pt sites and MoS_2 supports for high-efficiency room-temperature SO_2 sensing. Firstly, the introduced single Pt atoms can activate the whole S species on supports to form S vacancy-assisted single Pt sites (Pt-Vs) at reductive atmosphere (Fig. 1-①). Reversely, the activated S species can provide a feedback role in tailoring the antibonding-orbital electronic occupancy state of Pt atoms (Fig. 1-②). Detailedly, the assistant sulfur vacancy can elevate the d-band center position of the single Pt sites and reduce the occupation state of the Pt–S antibonding orbital, thus increasing the strength of the Pt–S bond and further improving the SO_2 adsorption. Gas adsorption/desorption experiments and in situ gas adsorption breakthrough experiments demonstrate sulfur vacancy-aided $\text{Pt}_1\text{-MoS}_2$ catalysts ($\text{Pt}_1\text{-MoS}_2\text{-def}$) exhibit the strongest SO_2 gas adsorption capacity. Ex situ X-ray photoelectron spectroscopy (XPS) and in situ Raman spectroscopy further experimentally confirm that the intact feedback-regulation system can expand the electron transfer path from single Pt

sites to whole Pt₁-MoS₂ supports in SO₂ gas atmosphere. This thus endows Pt₁-MoS₂-def sensors extremely low limit of detection (500 ppb) and high response sensitivity (3.14% to 500 ppb SO₂) at room temperature. At the same time, equipped with Bluetooth intelligent monitoring modules, the Pt₁-MoS₂-def sensors array can further realize real-time monitoring of SO₂ levels and cloud-data transmission/storage for plant growth.

2 Experimental Section

2.1 Materials

Chloroplatinic acid (H₂PtCl₆), ascorbic acid (AA), ammonium molybdate tetrahydrate ((NH₄)₆Mo₇O₂₄·4H₂O), aniline, L-Cysteine, hydrochloric acid (HCl) and ethanol

(C₂H₅OH) were analytical grade and purchased from Shanghai Chemical Corp. All reagents in the experiment were used without any further purification. All solutions were prepared in deionized water. Gases including hydrogen sulfide (H₂S), nitrous oxide (N₂O), xylene (C₈H₁₀), nitrogen dioxide (NO₂), nitric oxide (NO), hydrogen (H₂), ammonia (NH₃) and sulfur dioxide (SO₂) were obtained from Shanghai Shenkai Gases Technology Co., Ltd.

2.2 Preparation of Trimolybdate, MoS₂, MoS₂-def, Pt₁-MoS₂, Pt₁-MoS₂-def and Pt NPs-MoS₂

2.2.1 Preparation of Aniline Trimolybdate (MoO₃-ANE)

The MoO₃-ANE was synthesized following a previous report [28] with minor modification. First, 2.48 g of

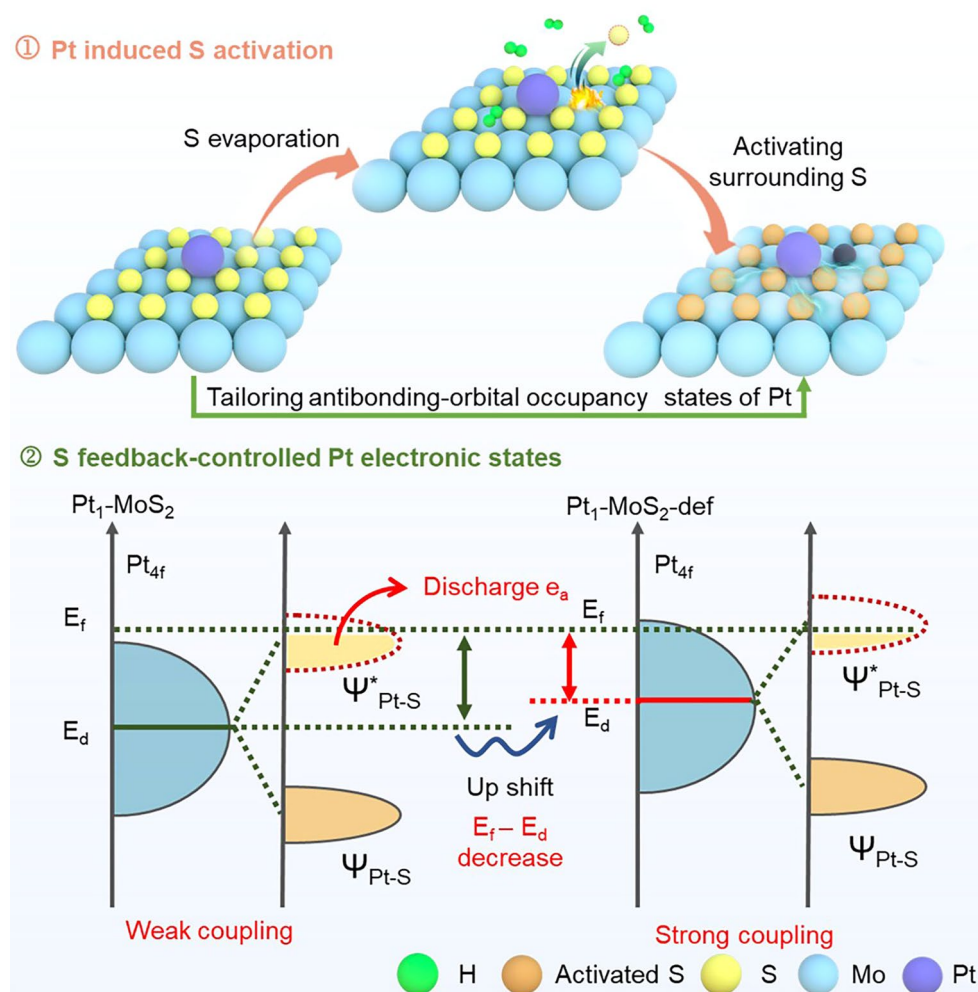


Fig. 1 The schematic of the feedback-regulation system in the Pt₁-MoS₂-def

$(\text{NH}_4)_6\text{Mo}_7\text{O}_{24}\cdot 4\text{H}_2\text{O}$ was dissolved in 50 mL of deionized water and 3.27 g of aniline was added. Then, 1 M HCl aqueous solution was added dropwise with magnetic stirring at room temperature until a white precipitate appeared (pH 4–5). After a reaction at 50 °C for 2 h, the product was filtered and thoroughly washed with ethanol, and then dried at 70 °C.

2.2.2 Preparation of Flower-Shaped MoS_2

The obtained MoO_3 -ANE (0.1 g) was dispersed in a homogeneous solution containing deionized water (15 mL) and L-Cysteine (0.2836 g). The dispersion solution was subsequently transferred to 50 mL Teflon-lined stainless-steel autoclaves and maintained at 200 °C for 14 h. The obtained samples were rinsed with ethanol and water and oven-dried at 70 °C for one day. Then, as-prepared powder was calcined in a tube furnace at 400 °C for 1 h at the heating rate of 2 °C min^{-1} under N_2 atmosphere.

2.2.3 Synthesis of MoS_2 -def

The obtained black powder of MoS_2 (200 mg) was treated in a tube furnace at 100 °C for 1 h under the 5% H_2/Ar_2 atmosphere at the heating rate of 2 °C min^{-1} . The final product MoS_2 -def was collected.

2.2.4 Synthesis of Pt_1 - MoS_2 , Pt_1 - MoS_2 -def and Pt NPs- MoS_2

The obtained black powder of MoS_2 (200 mg) was dispersed in aqueous solution of deionized water (25 mL) and ethanol (25 mL). An aqueous solution of chloroplatinic acid (10 mg mL^{-1} , 0.2 mL) was subsequently added into the dispersion and stirred for 24 h at room temperature. The precipitate was separated, washed and dried under vacuum at 70 °C for 24 h. The as-above precipitate was treated in a tube furnace at 100 °C for 1 h under the 5% H_2/Ar atmosphere at the heating rate of 2 °C min^{-1} . The final product Pt_1 - MoS_2 -def was collected. Pt_1 - MoS_2 was prepared with the same synthesis procedure of Pt_1 - MoS_2 -def except the tube furnace was not treated. The decoration of Pt (0.1 wt%) NPs was achieved through in situ reduction method. 200 mg as-prepared MoS_2 powder were subsequently dispersed in

25 mL ethanol and 25 mL deionized water. An aqueous solution of chloroplatinic acid (10 mg mL^{-1} , 30 μL) and 1 mL AA solution (0.1 M) were subsequently added into the dispersion and stirred for 24 h at room temperature. The product was precipitated by centrifugation and dried at 70 °C for overnight.

2.3 Characterizations

X-ray diffraction patterns (XRDs) were collected by using powder XRD (Rigaku D/MAX-2500 X-ray diffractometer, with $\text{Cu K}\alpha_1$ radiation $\lambda = 0.154056$ nm 40 kV and 40 mA, scanning from 10° to 70°). The microtopography of the synthesized materials was recorded with scanning electron microscopy (SEM, JSM-6700F) and high-resolution transmission electron microscopy (HRTEM, JEM-2100F, Japan). The high-resolution TEM and high-angle annular dark-field scanning TEM (HAADF-STEM) images were recorded on an FEI Tecnai G2 F20 S-Twin high-resolution transmission electron microscope (HRTEM; Hillsboro, OR, United States) set at 200 kV, and a JEOL JEM-ARM300F TEM/STEM (Tokyo, Japan), respectively, with a spherical aberration corrector worked at 300 kV. Through-focal HAADF series were acquired at nanometer intervals, with the first image under-focused (beyond the beam exit surface) and the final image over-focused (before the beam entrance surface). Then, the images were aligned manually to remove the sample drift effects. Electron paramagnetic resonance (EPR) spectra were recorded on a Bruker CW Eleksys E500 spectrometer by applying an X-band (9.4 GHz) microwave with sweeping magnetic field at room temperature.

3 Results and Discussion

3.1 Construction and Characterization of Pt_1 - MoS_2 and Pt_1 - MoS_2 -def

The MoS_2 were firstly synthesized by an anion-exchange strategy by using MoO_3 -ANE (aniline-functional MoO_3) as precursors (Fig. S1). The SEM, TEM and HRTEM images in Fig. S2 reveal a uniform hierarchical nanosheet configuration with a well-ordered lattice fringe spacing of 0.27 nm, which agrees well with the (100) facet of hexagonal molybdenum disulfide. Subsequently, the Pt species

were introduced through a deposition–precipitation process. As seen in Fig. S3, the high-angle annular dark-field scanning transmission electron microscopy (HAADF-STEM) image shows the atomic dispersion of Pt species over the Pt₁-MoS₂ surface and no notable Pt clusters are observed. Driven by thermal treatment of Pt₁-MoS₂ in a reductive atmosphere, Pt₁-MoS₂-def catalyst was synthesized. No remarkable architectonic changes and Pt nanoparticles are found (Fig. S4a, b). Meanwhile, the energy-dispersive X-ray spectroscopy (EDS) mapping (Fig. S4c) further demonstrates the homogeneous distribution of Pt, Mo and S elements. Furthermore, HAADF-STEM (Fig. 2a) clearly shows that the individual Pt atoms atomically disperse over the whole support surface without agglomerate, which is further confirmed by the extractive X–Y intensity profiles and atom-overlapping Gaussian-function fitting images of selective area scan (Fig. 2b–d). The simulating configuration (Fig. 2f) clearly exhibits the distribution of single dispersed Pt atoms, it is in accordance with the STEM image (Fig. 2e). For comparison, Pt nanoparticle modified MoS₂ (Pt NPs-MoS₂) was also synthesized through the ascorbic acid reduction in Fig. S5. More representative SEM, TEM, XRD and BET images of Pt₁-MoS₂, Pt₁-MoS₂-def, Pt NPs-MoS₂ are displayed in Figs. S6–S9. Moreover, the Pt loading contents of Pt₁-MoS₂-def and Pt NPs-MoS₂ are measured as 0.1% by inductively coupled plasma optical emission spectrometry (ICP-OES) (Table S1).

Element-selective X-ray absorption fine structure (XAFS) was further performed to explore the coordination environment of Pt species. As seen in Fig. 2g, the X-ray absorption near edge structure (XANES) spectra reveal the white line intensities of Pt₁-MoS₂-def and Pt₁-MoS₂ peaks are located between the PtS₂ and Pt foil, suggesting the oxidation state of Pt^{δ+} (0 < δ < 4). The Fourier transferred extended X-ray absorption fine structure (FT-EXAFS) in Fig. 2h displays two notable peaks at ~1.90 Å, which are contributed by the Pt–S coordination path. No Pt–Pt characteristic peak (at ~2.57 Å) is detected for both Pt₁-MoS₂-def and Pt₁-MoS₂ samples, confirming the atomic dispersion of Pt on the supports. Moreover, the first-shell EXAFS fitting curves (Fig. 2i) and corresponding fitting results (Fig. S10 and Table S2) validate that the central Pt atom in both Pt₁-MoS₂ and Pt₁-MoS₂-def samples directly coordinates with three S atoms with the average bond lengths of 2.32 and 2.33 Å, respectively. Moreover, the wavelet transforms spectra of Pt EXAFS oscillations in Fig. 2j display only one peak at

7 Å⁻¹ for Pt₁-MoS₂-def and Pt₁-MoS₂ samples, regarded as the Pt–S coordination contribution, indicating the high-distributed status of single Pt species.

3.2 Feedback-regulation System of Pt₁-MoS₂-def

The first-principal calculations were further conducted to verify the Pt-site configuration on the support. Figure 3a simulates the diffusion path of the Pt atom on the MoS₂ surface, including ⊕Pt on the S site, ⊙Pt on the hollow site and ⊚Pt on the Mo site. The results of the DFT calculation (Fig. S11) show that the Pt atom can stabilize on the top of the Mo site with the lowest binding energy of –3.265 eV in contrast to –2.764 eV (Pt on the S site) and 6.024 eV (Pt on the hollow site). Also, this configuration of Pt atom bonding with three S atoms is consistent with the XAFS fitting results. After further treating the Pt₁-MoS₂ in a reduced atmosphere, the S atoms will spontaneously escape from the MoS₂ surface to generate sulfur vacancy sites (Pt₁-MoS₂-def). This process will induce five potential configurations in Fig. S12. Considering the adjudication of experimental investigations (detailed descriptions in supporting information), the defect 2 model (adjacent non-bonding S defect) was selected as the optimal configuration with the lowest vacancy formation energy of –1.876 eV. This spontaneous reaction process (Fig. S13) indicates that the introduced single Pt atom can promote the evaporation of adjacent S species. Importantly, this three-coordinated structure of Pt₁-MoS₂-def is also well conforming by XAFS results. Furthermore, the theoretical deduction can be verified by the experimental electron paramagnetic resonance (EPR) analysis. As shown in (Fig. 3b), the signal intensity of sulfur vacancies (at g = 2.003) of Pt₁-MoS₂-def is significantly higher than that of MoS₂-def [29] (more synthetic process showed in supporting information), demonstrating single Pt atoms can induce the formation of sulfur vacancies and thus activate the whole S plane.

The XPS measurements are employed to unveil the chemical environment of Mo (Fig. 3c), S (Fig. 3d) and Pt (Fig. 3e) species. As shown in Fig. 3c, the peaks at 231.9 eV (Mo 3d_{3/2}) and 228.7 eV (Mo 3d_{1/2}) are attributed to Mo⁴⁺ and the peaks at 233.9 eV (Mo 3d_{3/2}) and 230.7 eV (Mo 3d_{1/2}) are assigned to Mo⁵⁺ [30], respectively. After introducing the Pt species, the doublet peaks of both Mo⁴⁺ (232.1 and 228.9 eV) and S²⁻ (161.9 and

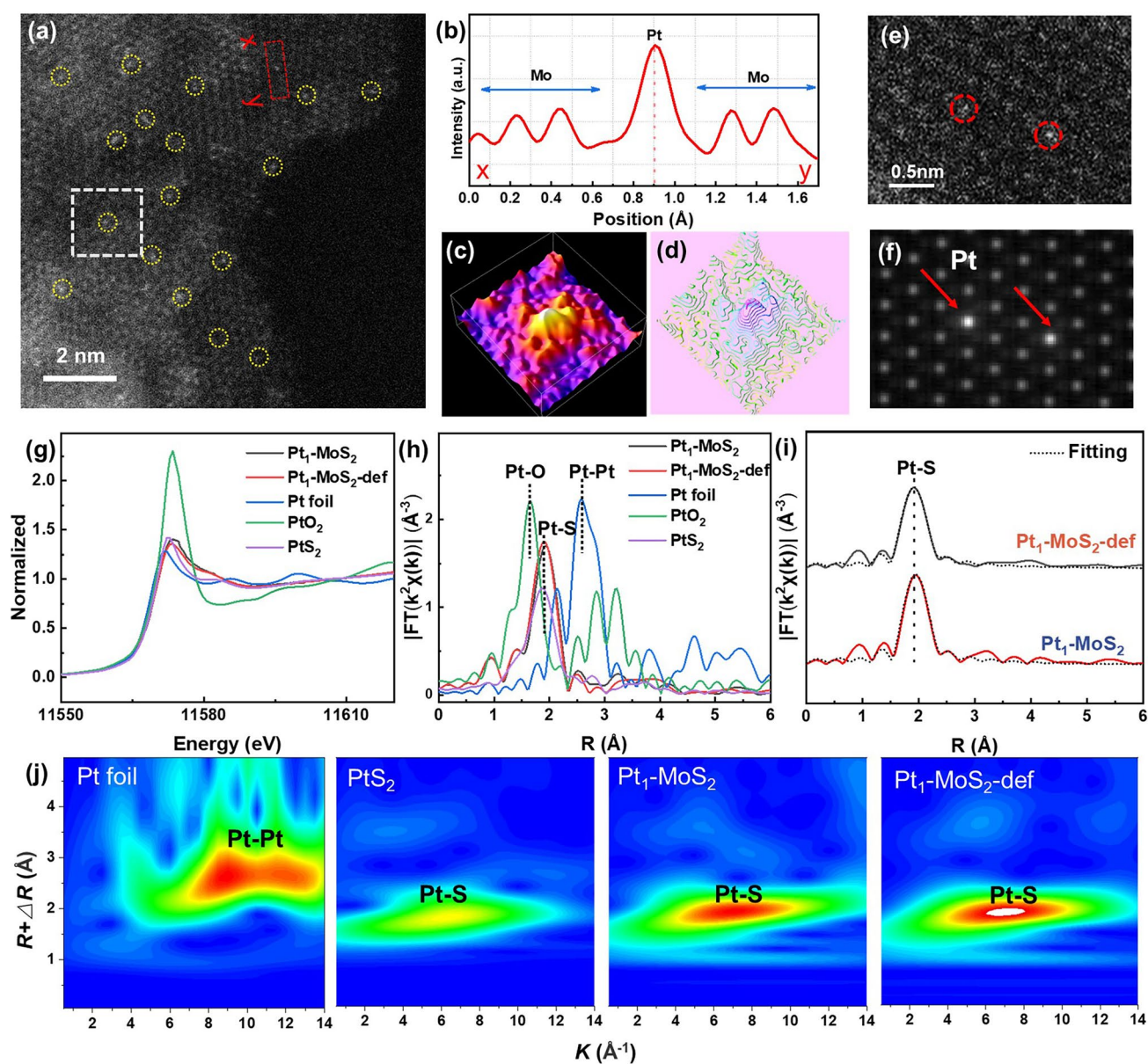


Fig. 2 Characterization of $\text{Pt}_1\text{-MoS}_2$ and $\text{Pt}_1\text{-MoS}_2\text{-def}$. **a** HAADF-STEM image of $\text{Pt}_1\text{-MoS}_2\text{-def}$. **b** The intensity profiles obtained in regions X–Y in **(a)**. **c, d** The atom-overlapping Gaussian-function fitting images of selective area scan (measured from white frame of **(a)**). **e, f** HAADF-STEM image of $\text{Pt}_1\text{-MoS}_2\text{-def}$ and its simulated image. **g** Pt L-edge XANES spectra. **h** FT-EXAFS spectra and **i** corresponding fitting curve of Pt L_3 edge. **j** Wavelet transform patterns of Pt foil, PtS_2 , $\text{Pt}_1\text{-MoS}_2$ and $\text{Pt}_1\text{-MoS}_2\text{-def}$

163.2 eV) in the $\text{Pt}_1\text{-MoS}_2$ shift to higher binding energy (0.2 and 0.3 eV left shifts, respectively) compared with pure MoS_2 . Meanwhile, the binding energy of Pt 4f peak is higher than Pt^0 (71.2 eV, Fig. S14) but lower than that of Pt^{4+} (74.0 eV) [26] according to the XAFS results. For $\text{Pt}_1\text{-MoS}_2\text{-def}$ catalysts, the double peaks of Mo^{5+} (233.9 and 230.7 eV) and the high valence S^{n+} peaks

(164.5 and 169.2 eV) gradually disappear. The Pt peaks in $\text{Pt}_1\text{-MoS}_2\text{-def}$ (72.8 eV) shift toward lower binding energy (0.3 eV) in contrast to the $\text{Pt}_1\text{-MoS}_2$ sample. The theoretical planar-averaged electron density difference $\Delta\rho(z)$ and Bader charge transfer in Fig. 3f further verify that the Pt atom in the as-established $\text{Pt}_1\text{-MoS}_2\text{-def}$ model can reduce the electronic loss toward supports, according

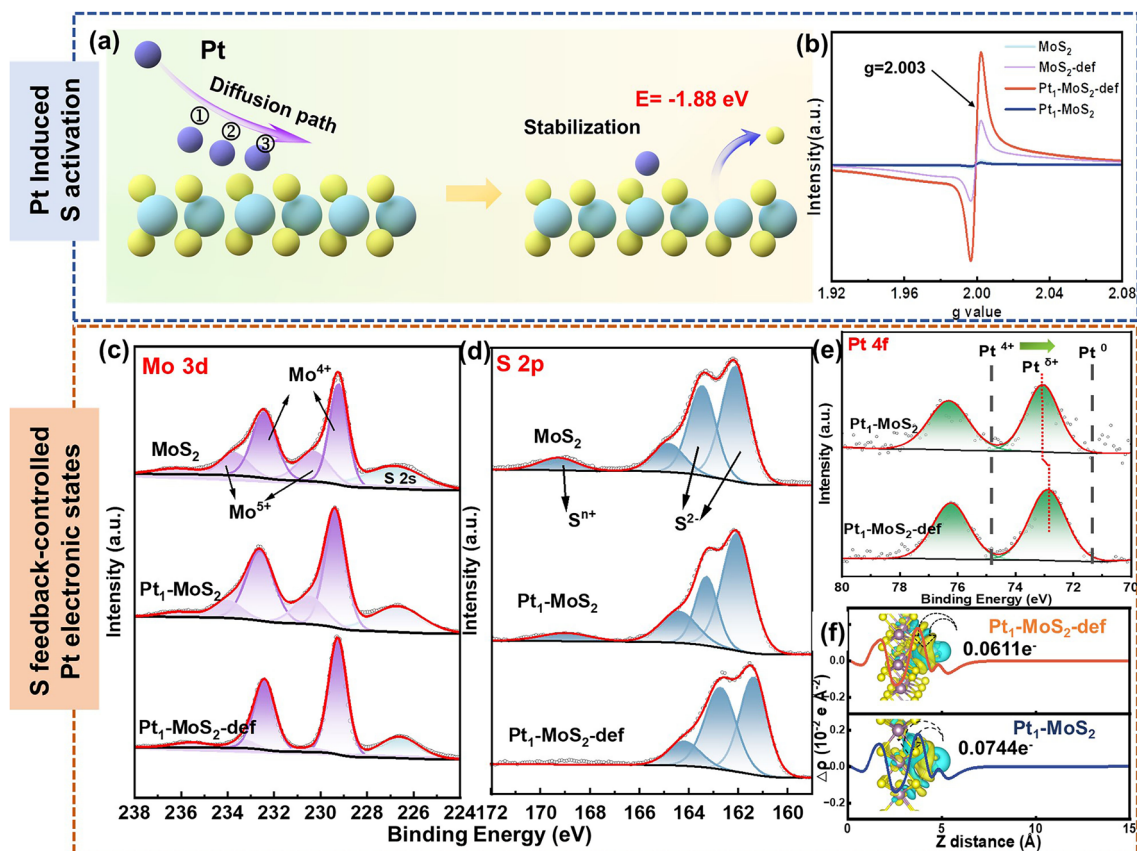


Fig. 3 Structural characterizations of Pt₁-MoS₂-def and reference materials. **a** The diffusion path of Pt atoms on MoS₂-def surface and diagram of S vacancy formation energy. **b** Electron-paramagnetic resonance images of MoS₂, MoS₂-def, Pt₁-MoS₂ and Pt₁-MoS₂-def. **c** Mo 3d XPS of MoS₂, Pt₁-MoS₂ and Pt₁-MoS₂-def. **d** S 2p XPS of MoS₂, Pt₁-MoS₂ and Pt₁-MoS₂-def. **e** Pt 4f XPS of Pt₁-MoS₂ and Pt₁-MoS₂-def. **f** The planar-averaged electron density difference $\Delta\rho(z)$ of Pt₁-MoS₂ and Pt₁-MoS₂-def

well to experimental XPS investigation. Both experimental and theoretical results reveal that activated S species will provide a feedback role in tailoring the electronic states of Pt atoms. In conclusion, the single Pt sites on the MoS₂ surface can induce easier volatilization of adjacent S species and the activated S species can inversely impact the electronic configuration of Pt atoms, thus leading an intact feedback-regulation system.

3.3 Sensing Properties and Mechanism of MoS₂, Pt₁-MoS₂ and Pt₁-MoS₂-def

The sensing properties of the MoS₂, Pt₁-MoS₂ and Pt₁-MoS₂-def MEMS sensors were investigated at room temperature (RT). The dynamic response transitions curves of the sensors along with SO₂ concentrations in the range of 0.5–40 ppm are exhibited in Fig. 4a, b. Obviously, the

Pt₁-MoS₂-def sensor displays the highest response values toward different concentrations of SO₂ compared with Pt₁-MoS₂ and MoS₂ sensors. Some baseline drift of the three sensors at room temperature could be attributed to the incomplete desorption of the SO₂ molecule [31]. Especially, the Pt₁-MoS₂-def sensors (25% to 5 ppm SO₂) exhibit an enhanced response approximately four times and five times higher than that of Pt₁-MoS₂ (7% to 5 ppm SO₂) sensors and MoS₂ sensors (5% to 5 ppm SO₂), respectively. Figure 4c shows the linear relationships between responses and SO₂ concentrations within 0.5–40 ppm for three sensors. Impressively, the Pt₁-MoS₂-def sensors exhibit an exceptional linear section with increased SO₂ concentrations, while the MoS₂ sensors endure the erratic response-concentration relationship. Additionally, the experimental limit of detection (LOD) of the Pt₁-MoS₂-def sensor can reach as low as 500 ppb, whereas the Pt₁-MoS₂ sensors and

MoS₂ sensors cannot perceive SO₂ gas below 1 ppm. Such a distinguished response performance exceeds that of Pt NPs-MoS₂ sensors (Fig. S15) and most reported SO₂ sensors (Fig. 4d and Table S4). More dynamic response-recovery resistance curves of MoS₂, Pt₁-MoS₂ and Pt₁-MoS₂-def sensors are shown in Fig. S16. As shown in Fig. 4e, eight

kinds of typical vaporous molecules including sulfur dioxide (SO₂), ammonia (NH₃), hydrogen (H₂), sulfuretted hydrogen (H₂S), nitric oxide (NO), xylene (C₈H₁₀), nitrogen dioxide (NO₂) and nitrous oxide (N₂O) were detected at the same concentration of 5 ppm at RT. It is found that the responses of interfering gases are significantly negligible.

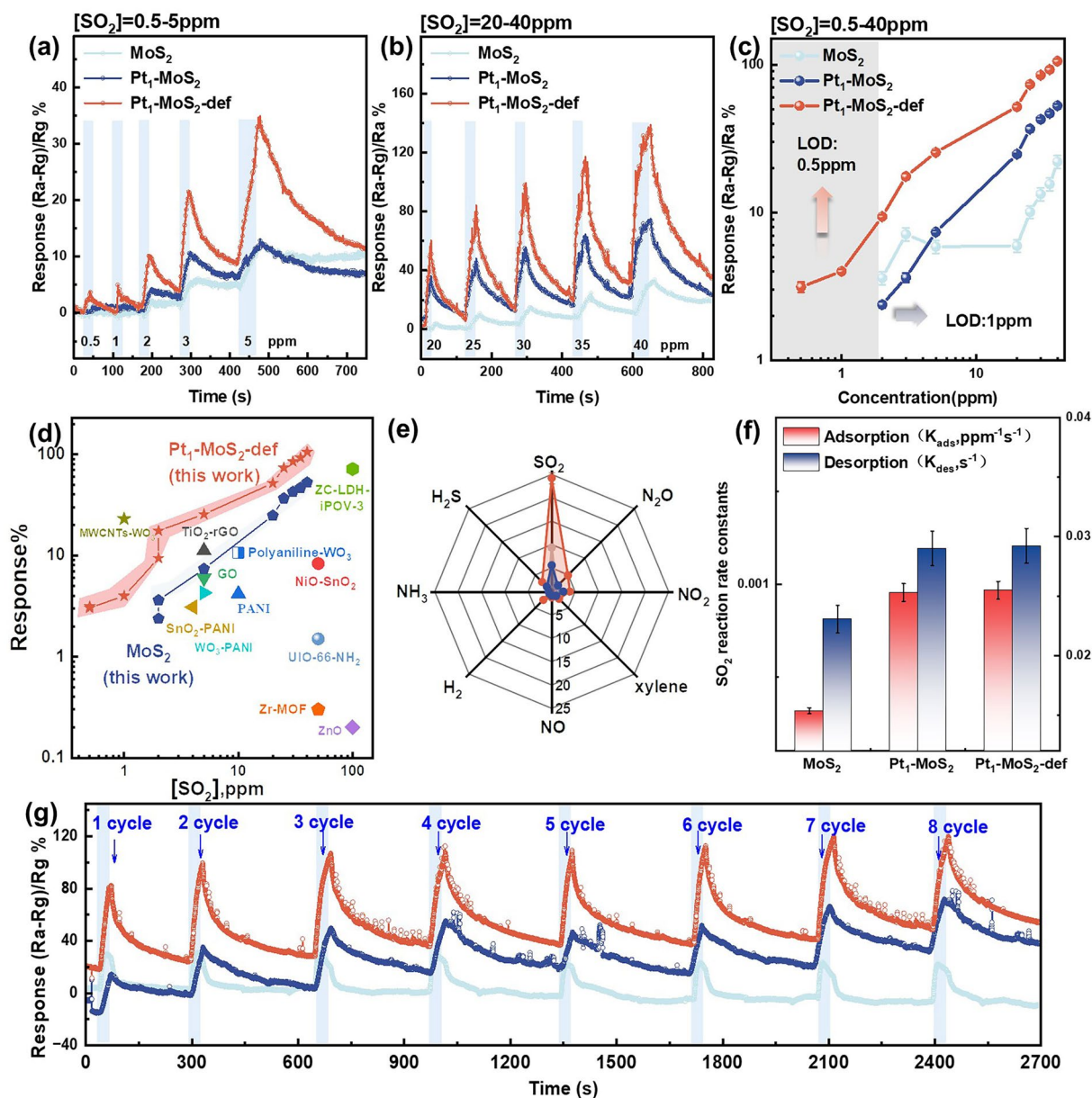


Fig. 4 Gas-sensing performance of MoS₂, Pt₁-MoS₂ and Pt₁-MoS₂-def. **a, b** Time-related dynamic responses in the concentration range of 0.5–5 and 20–40 ppm. **c** The responses of MoS₂, Pt₁-MoS₂ and Pt₁-MoS₂-def in different SO₂ concentrations. **d** RT operation state-of-the-art SO₂ chemiresistors for response. **e** The selectivity of MoS₂, Pt₁-MoS₂ and Pt₁-MoS₂-def in different gases. **f** Adsorption and desorption rate constant K_{ads} and K_{des} values. **g** stability tests using sensors upon 8 cyclic exposures to 25 ppm SO₂. (All the sensing tests were conducted at RT in (30%RH) condition)

Furthermore, the calculated selectivity coefficients (K) of all sensors (Fig. S17) reveal relatively high K values, indicating excellent SO_2 selectivity for gas-sensing performances. The adsorption (k_{ads}) and desorption (k_{des}) rate constants of all sensors (Fig. 4f) were further calculated by fitting the response versus time curves (Fig. S18) using the equations below:

$$R(t) \text{ for } \text{SO}_2 \text{ adsorption} = R_{\text{max}} \cdot \frac{C_a K}{1 + K C_a} \left(1 - e^{\left[-\frac{1-KC_a}{K} \cdot k_{\text{ads}} t \right]} \right) \quad (1)$$

$$R(t) \text{ for } \text{SO}_2 \text{ desorption} = R_0 e^{[-k_{\text{des}} t]} \quad (2)$$

where R_{max} is the maximum response value, R_0 is the response in air, C_a is the concentration of SO_2 gas, t is the time and K is the equilibrium constant ($k_{\text{ads}}/k_{\text{des}}$) [32]. The results indicate that the kinetic adsorption and desorption of SO_2 molecules are promoted by Pt species and sulfur vacancies. In addition, the cycle stability (Fig. 4g) and long-term durability measurements (Fig. S19) show that the $\text{Pt}_1\text{-MoS}_2\text{-def}$ sensor can remain almost unchanged responses during continuous eight-cyclical exposure of SO_2 and superior stability for up to 35 days. The effects of operating temperature for $\text{Pt}_1\text{-MoS}_2\text{-def}$ sensor were conducted in Fig. S21, in which the sensors can realize optimal gas-sensing performance at room-temperature conditions. Besides, the resistances of the $\text{Pt}_1\text{-MoS}_2\text{-def}$ sensor may be affected by the humidity environment (Fig. S22), which is mainly because water molecules might react with SO_2 molecules. A water filtration membrane to filter out water molecules was added on the device (Fig. S23a). As shown in Fig. S23b, c, after adjusting the device, the response of the material to 25 ppm SO_2 under different humidity conditions were tested. It was observed that under 90% humidity, the sensor's response decreased by no more than 9% (before the improvement, the sensor's response decreased by about 28%), effectively improving the normal operation of the device in high humidity environments.

To further clear the design superiority of the $\text{Pt}_1\text{-MoS}_2\text{-def}$ catalysts in the gas-sensing reaction, SO_2 adsorption and desorption tests were implemented (experimental details are shown in Methods and Table S3). As Fig. 5a–c shows, the $\text{Pt}_1\text{-MoS}_2\text{-def}$ reveals the maximum adsorption capacity (2.34 wt%) and the fastest average adsorption rate (0.52 wt% s^{-1}) for SO_2 compared with MoS_2 (1.32 wt%, 0.18 wt% s^{-1}), $\text{Pt}_1\text{-MoS}_2$ (1.62 wt%, 0.41 wt% s^{-1}) and Pt NPs- MoS_2 (1.75 wt%, 0.44 wt% s^{-1}) at room temperature, indicating the S vacancy-assisted single Pt sites (Pt-Vs) can induce superior adsorption and excitation ability for sulfur dioxide. Ex situ

XPS spectra were further employed to investigate the reaction mechanism of different catalysts. As seen in Fig. 5d, the peaks of Pt^{4+} in $\text{Pt}_1\text{-MoS}_2$ suddenly appear in the SO_2 atmosphere while no obvious new peaks are found in the Mo and S species, confirming the electron transfer path is from the single Pt site to adsorbed SO_2 molecule. However, a small number of surface-adsorbed SO_2 molecules are not distinguished by the XPS detection. Same results can also be found in $\text{MoS}_2\text{-def}$ catalysts in Fig. S24. Considering the resistances of MoS_2 -based sensors significantly reduce in the oxidizing SO_2 atmosphere (Fig. S25), the sensing type can be identified as p-type semiconductors. Detailly, the SO_2 species can capture electrons from the conduction band of p-type semiconductors and induce the hole generation, resulting in decreased resistances (Fig. S26). For the $\text{Pt}_1\text{-MoS}_2\text{-def}$ catalyst (Fig. 5e), two new higher-valence S peaks (168.83 and 170.1 eV, S^{6+}) and Pt^{4+} peaks are discovered after SO_2 treatment while there is a slight high binding energy shift in the Mo 3d spectrum, revealing that both Pt and MoS_2 supports lose electrons during the gas-sensing process. The in situ Raman spectra display the 150 s exposure periods of $\text{Pt}_1\text{-MoS}_2\text{-def}$, $\text{Pt}_1\text{-MoS}_2$ (Fig. 5f) and $\text{MoS}_2\text{-def}$ (Fig. S27) after treating with 1000 ppm SO_2 . Clearly, the A_{1g} peak (at 402.25 cm^{-1}) of the $\text{Pt}_1\text{-MoS}_2\text{-def}$ sample shifts to a higher wavenumber after SO_2 exposure for 60 s, while no peak changes for the $\text{Pt}_1\text{-MoS}_2$ and $\text{MoS}_2\text{-def}$ samples. Therefore, this unequivocally corroborates that the electronic transform process in $\text{Pt}_1\text{-MoS}_2\text{-def}$ involves the adsorbed SO_2 molecules and the whole supports. In conclusion, experimental results demonstrate there are two potential reaction paths dominant to the SO_2 sensing performance for $\text{Pt}_1\text{-MoS}_2\text{-def}$ and $\text{Pt}_1\text{-MoS}_2$ sensors. For $\text{Pt}_1\text{-MoS}_2$ (Fig. 5g, type I), the electrons mainly locate around the single Pt site and the electron transfer only occurs within Pt–S (SO_2). In comparison, the $\text{Pt}_1\text{-MoS}_2\text{-def}$ sensors contain synergistically single Pt sites and activated inert S plane, which prompts the whole supporting surface to participate in the SO_2 sensing process (Fig. 5g, type II). Meanwhile, the rapid electron transfer between $\text{Pt}_1\text{-MoS}_2\text{-def}$ and the oxidizing SO_2 guarantees high response and low LOD. In addition, the in situ SO_2 adsorption breakthrough curves (Fig. 5h) were implemented to quantitatively measure the absorption of SO_2 , in which the adsorbed SO_2 amounts on $\text{Pt}_1\text{-MoS}_2\text{-def}$ is 281 $\mu\text{mol g}^{-1}$ more than that on $\text{Pt}_1\text{-MoS}_2$, and there is 292 $\mu\text{mol g}^{-1}$ more than that on $\text{MoS}_2\text{-def}$ at 25 °C, according well with the SO_2 adsorption and desorption tests in Fig. 5a–c.

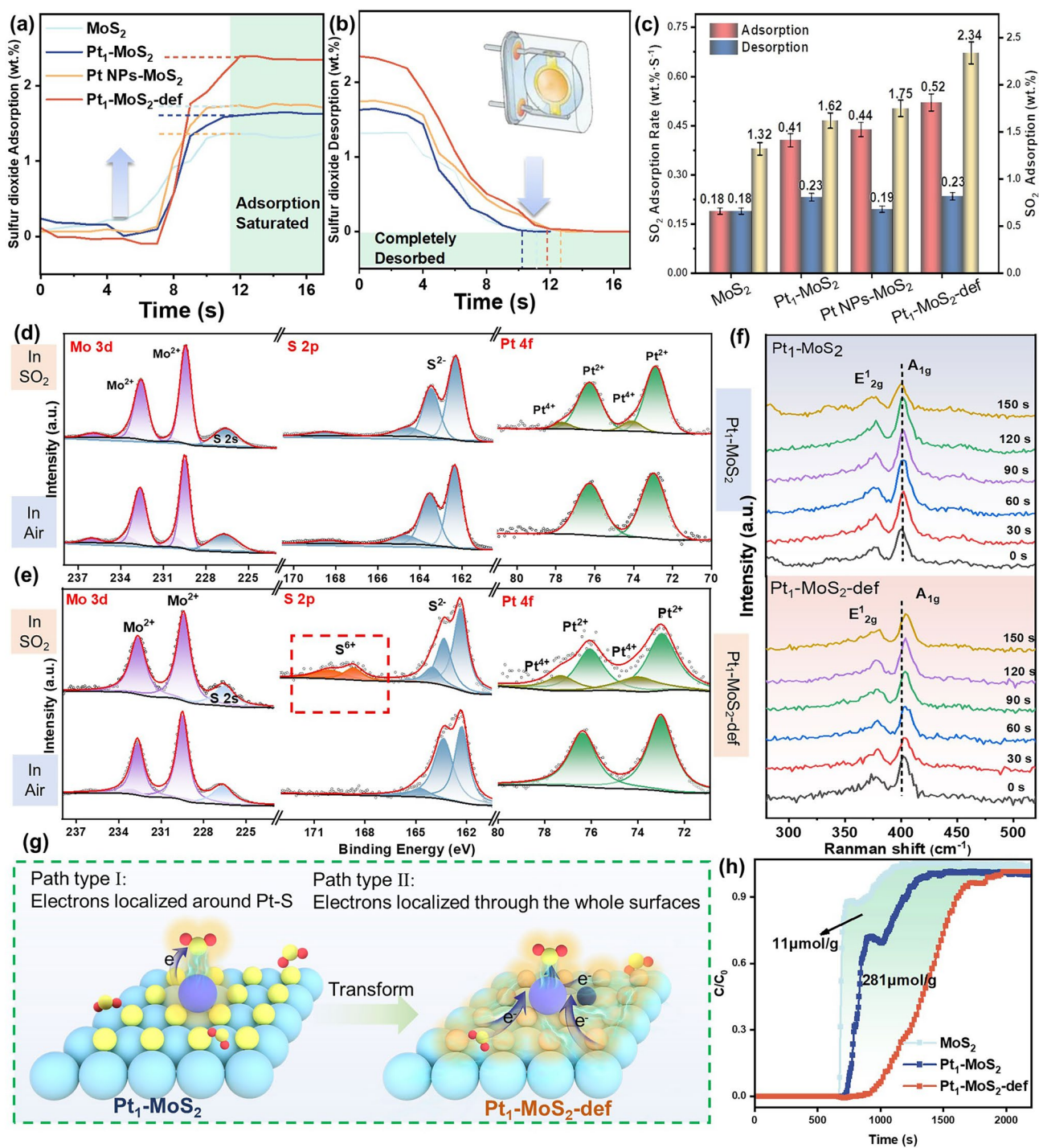


Fig. 5 The experimental investigation of the mechanism for the gas-sensing property of Pt₁-MoS₂-def. **a** The SO₂ adsorption curves, **b** desorption curves and **c** SO₂ adsorption rate of MoS₂, Pt₁-MoS₂, Pt NPs-MoS₂ and Pt₁-MoS₂-def. The ex situ XPS spectra of **d** Pt₁-MoS₂ and **e** Pt₁-MoS₂-def. **f** In situ Raman spectra of the Pt₁-MoS₂ and Pt₁-MoS₂-def. **g** Two different path types of Pt₁-MoS₂ and Pt₁-MoS₂-def with SO₂. **h** In-situ SO₂ adsorption breakthrough curves of MoS₂, Pt₁-MoS₂ and Pt₁-MoS₂-def at 25 °C

3.4 Theoretical Investigations

DFT calculations were conducted to explore the structure–activity relationships between single Pt sites and gas-sensing performance. As seen in Fig. 6a, the Pt 4d partial DOS (pDOS) results show that the d-band center in Pt₁-MoS₂-def (-2.58 eV) obviously upshifts compared with the Pt₁-MoS₂ (-4.10 eV). The corresponding DOS images are displayed in Fig. S28. When interacting with SO₂ molecule, the Pt–S (SO₂) projects crystal orbital Hamilton

population (pCOHP) is calculated in Fig. 6b, where the negative –pCOHP represents the antibonding contribution and the positive –COHP stands for bonding contribution [33–35]. Obviously, the antibonding contribution gradually moves upward (compared to E_f) from Pt₁-MoS₂-def to Pt₁-MoS₂, proving a decreased occupation state and a strengthening Pt–S bond. The –IpCOHP (the integral of –COHP up to the Fermi level) values are further calculated in Fig. 6c. The antibonding orbital occupation state of the Pt–S bond in Pt₁-MoS₂-def is smaller than that in Pt₁-MoS₂,

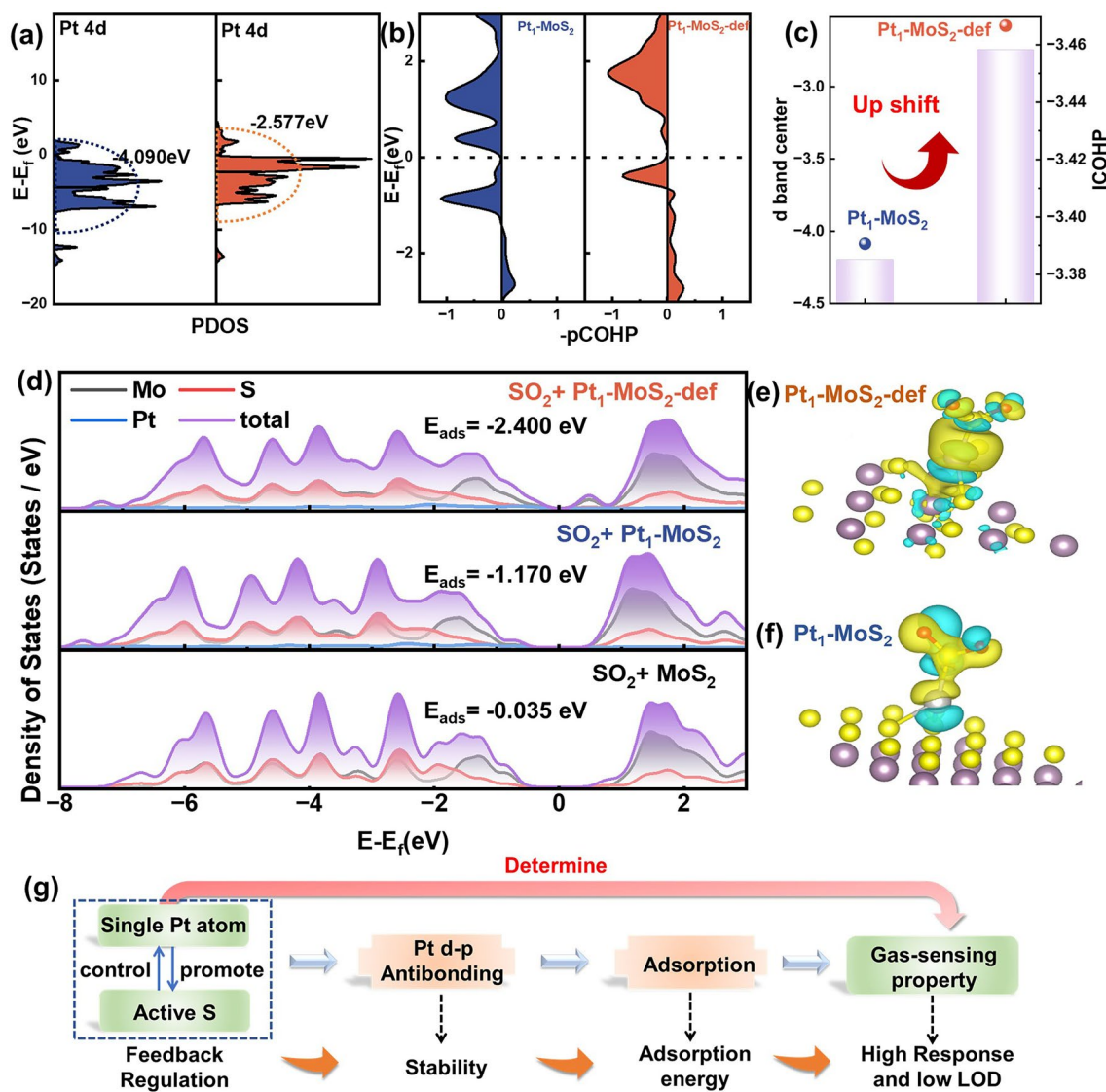


Fig. 6 The theoretical investigation of the mechanism for the gas-sensing property of Pt₁-MoS₂-def. **a** pDOS for Pt 4d orbital and the d band center of Pt₁-MoS₂ and Pt₁-MoS₂-def. **b** pCOHP and **c** ICOHP of terminal Pt–S bonds of Pt₁-MoS₂ and Pt₁-MoS₂-def. **d** The partial density of states (pDOS) analysis and adsorption energy of SO₂/Pt₁-MoS₂-def, SO₂/Pt₁-MoS₂ and SO₂/MoS₂ models. The electronic transfer between SO₂ and **e** Pt₁-MoS₂-def and **f** Pt₁-MoS₂ sample. The yellow and blue lobes represent the accumulation and depletion of charge. **g** Mechanism for tailoring the level of antibonding-orbital occupancy state to unidirectionally determined the gas-sensing property of SO₂

indicating more stable adsorption of SO_2 for $\text{Pt}_1\text{-MoS}_2\text{-def}$, which is conformed to the d-band center theory. In addition, the density of states (DOS) analysis in Fig. 6d displays that a new peak around Fermi energy level could be observed in $\text{SO}_2/\text{Pt}_1\text{-MoS}_2\text{-def}$, suggesting more electrons transfer between SO_2 and $\text{Pt}_1\text{-MoS}_2\text{-def}$ compared with $\text{SO}_2/\text{Pt}_1\text{-MoS}_2$ and SO_2/MoS_2 models. This can be further verified by the differential charge density comparisons in Fig. 6e, f. Also, the $\text{Pt}_1\text{-MoS}_2\text{-def}$ reveals larger the adsorption energy (E_{ads}) of -2.40 eV than that of the $\text{Pt}_1\text{-MoS}_2$ (-1.17 eV) and MoS_2 (-0.035 eV) upon interaction with SO_2 molecules (Fig. S29), according well with gas-sensing performance. Overall, utilizing Pt species to promote adjacent S evaporation, the electronic state of S vacancy-assisted single Pt

atom pronouncedly changes and thus induces a gradually decreased antibonding contribution state of Pt-S and a stronger SO_2 adsorption. Hence, the establish of feedback-regulation system is crucial for SO_2 -sensing material with high response and low LOD (Fig. 6g).

3.5 Bluetooth-Based Devices for Monitoring the Environment of Plant Growth

As we all known, the real-time monitor, track and prediction of stressful circumstances (such as SO_2) is of vital importance to optimize and adjust plant growth [8]. For instance, an appropriate SO_2 environment can promote seed germination and stomatal movement, while excessive SO_2

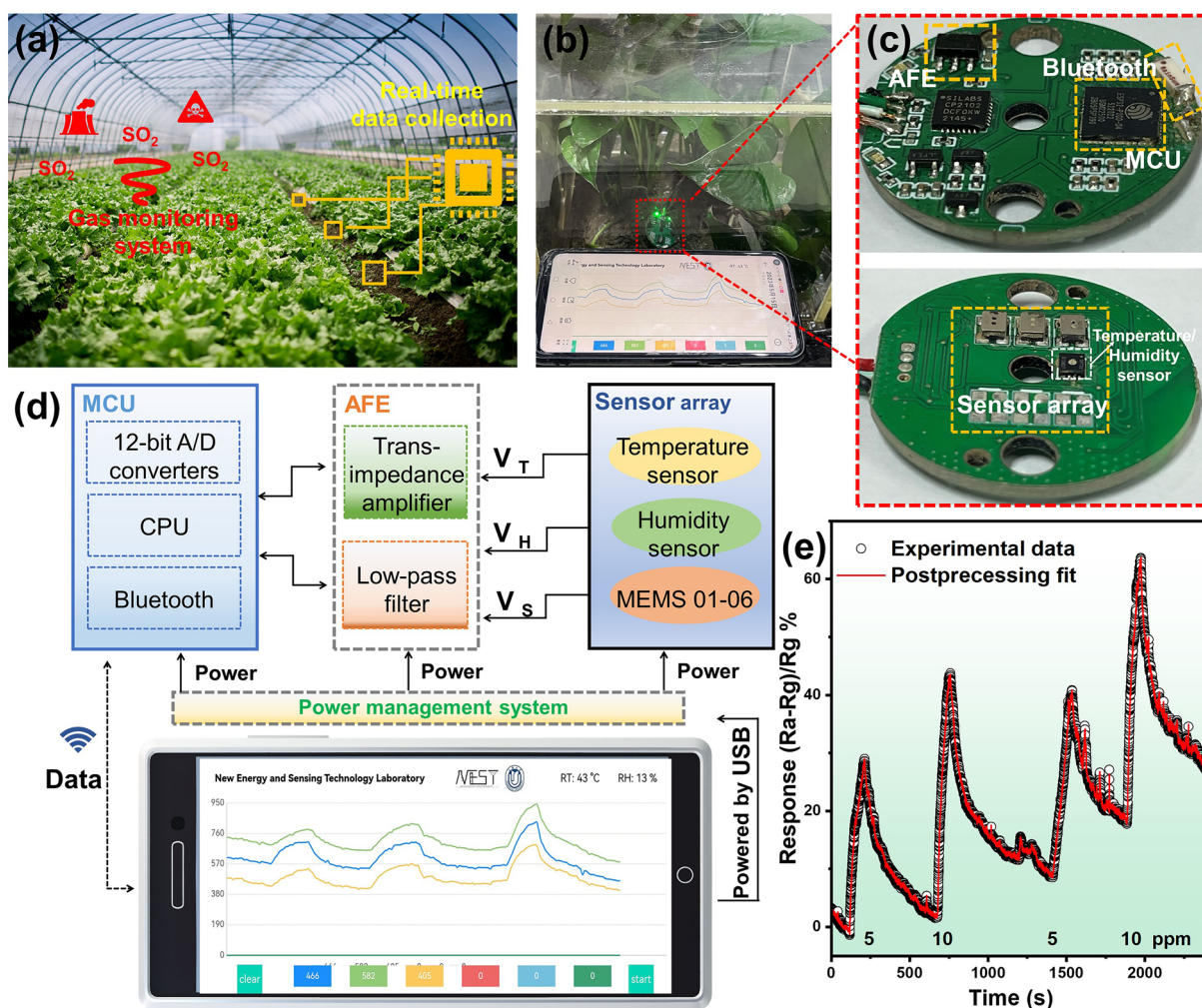


Fig. 7 $\text{Pt}_1\text{-MoS}_2\text{-def}$ -based SO_2 gas sensors for monitoring the plants growth. **a** Schematic of real-time detection of SO_2 gas concentration in a greenhouse. **b** Photo of the device in a simulated greenhouse with plants, with a smartphone and Bluetooth and data transmission. **c** Corresponding block modules. **d** Block diagram of the whole system. **e** Data measured by this device

concentrations will disturb the physiological and biochemical metabolism [36–38]. Therefore, engineering multifunctional SO₂ sensors array to timely collect and transmit the gas/temperature/humidity signals is desired for plant cultivation process (Fig. 7a). Based on the superior SO₂-sensing materials of Pt₁-MoS₂-def, a miniaturized, integrated and wireless sensing SO₂ sensors device is further developed in Fig. 7b, c. The disk-shaped device is composed of Bluetooth, Active Front End (AFE) and Micro Controller Unit (MCU) on one side, while a MEMS array (containing six sensors) and temperature/humidity modules are embedded at the back. Wireless data transmission from devices to smartphones can be achieved through the Bluetooth system. The corresponding block diagram is presented in Fig. 7d, including the power delivery, data conditioning and data transmission pathways. Impressively, synchronous six sensing signals can be received and revealed on the screen to calibrate the errors. More details of printed circuit board and the main interfaces of the custom mobile application device are shown in Figs. S30–S33. Furthermore, the portable sensing device displays constant responses for 5 and 10 ppm SO₂ gases (Fig. 7e) in a realistic greenhouse environment. More gas-sensing performance tests are shown in Fig. S34. Notably, the current design still stays in a proof-of-concept stage, it may require more optimizing process including signal handling, data integration, intellectual detection and so on in future work.

4 Conclusions

In summary, by designing the feedback-regulation system in Pt₁-MoS₂-def sensing materials, the superior SO₂ wireless detection sensors can be realized. When introducing the single Pt atom to MoS₂ surface, the adjacent S species is inclined to evaporate to form S vacancy-assisted single Pt sites. Reversely, the electronic state of Pt atom pronouncedly changes by the activated S planes. After treating with SO₂ gas, the antibonding contribution states of Pt–S gradually decreased and thus induce a stronger SO₂ adsorption. This result can further be confirmed by the gas adsorption/desorption experiments and in situ gas adsorption breakthrough experiments. The final Pt₁-MoS₂-def sensors show extremely high performance for low-concentration SO₂ gas sensing at room temperature (3.14% to 500 ppb). Combined with a Bluetooth transmission

system, the Pt₁-MoS₂-def sensor arrays can further achieve real-time SO₂ monitoring and data transmission under real conditions for plant growth. Our work is thus expected to broaden the rational design of highly effective gas sensors.

Acknowledgements This work was supported by the National Natural Science Foundation of China (62271299) and Shanghai Sailing Program (22YF1413400). Shanghai Engineering Research Center for We thank the Integrated Circuits and Advanced Display Materials.

Declarations

Conflict of interest The authors declare no interest conflict. They have no known competing financial interests or personal relationships that could have appeared to influence the work reported in this paper.

Open Access This article is licensed under a Creative Commons Attribution 4.0 International License, which permits use, sharing, adaptation, distribution and reproduction in any medium or format, as long as you give appropriate credit to the original author(s) and the source, provide a link to the Creative Commons licence, and indicate if changes were made. The images or other third party material in this article are included in the article's Creative Commons licence, unless indicated otherwise in a credit line to the material. If material is not included in the article's Creative Commons licence and your intended use is not permitted by statutory regulation or exceeds the permitted use, you will need to obtain permission directly from the copyright holder. To view a copy of this licence, visit <http://creativecommons.org/licenses/by/4.0/>.

Supplementary Information The online version contains supplementary material available at <https://doi.org/10.1007/s40820-024-01350-3>.

References

1. M. Kermani, S. Fallah Jokandan, M. Aghaei, F. Bahrami Asl, S. Karimzadeh et al., Estimation of the number of excess hospitalizations attributed to sulfur dioxide in six major cities of Iran. *Health Scope* **5**, e38736 (2016). <https://doi.org/10.17795/jhealthscope-38736>
2. Y. Wu, R. Li, L. Cui, Y. Meng, H. Cheng et al., The high-resolution estimation of sulfur dioxide (SO₂) concentration, health effect and monetary costs in Beijing. *Chemosphere* **241**, 125031 (2020). <https://doi.org/10.1016/j.chemosphere.2019.125031>
3. G. Goudarzi, S. Geravandi, E. Idani, S. Ahmad Hosseini, M.M. Baneshi et al., An evaluation of hospital admission respiratory disease attributed to sulfur dioxide ambient concentration in Ahvaz from 2011 through 2013. *Environ. Sci. Pollut. Res. Int.* **23**, 22001–22007 (2016). <https://doi.org/10.1007/s11356-016-7447-x>

4. D.-D. Lee, D.-S. Lee, Environmental gas sensors. *IEEE Sens. J.* **1**, 214–224 (2001). <https://doi.org/10.1109/JSEN.2001.954834>
5. T. Shaymurat, Q. Tang, Y. Tong, L. Dong, Y. Liu, Gas dielectric transistor of CuPc single crystalline nanowire for SO₂ detection down to sub-ppm levels at room temperature. *Adv. Mater.* **25**(2269–2273), 2376 (2013). <https://doi.org/10.1002/adma.201204509>
6. Z. Zhai, X. Zhang, J. Wang, H. Li, Y. Sun et al., Washable and flexible gas sensor based on UiO-66-NH₂ nanofibers membrane for highly detecting SO₂. *Chem. Eng. J.* **428**, 131720 (2022). <https://doi.org/10.1016/j.cej.2021.131720>
7. M. Balaish, J.L.M. Rupp, Widening the range of trackable environmental and health pollutants for Li-garnet-based sensors. *Adv. Mater.* **33**, e2100314 (2021). <https://doi.org/10.1002/adma.202100314>
8. G. Lee, Q. Wei, Y. Zhu, Emerging wearable sensors for plant health monitoring. *Adv. Funct. Mater.* **31**, 2106475 (2021). <https://doi.org/10.1002/adfm.202106475>
9. A.V. Agrawal, N. Kumar, M. Kumar, Strategy and future prospects to develop room-temperature-recoverable NO₂ gas sensor based on two-dimensional molybdenum disulfide. *Nano-Micro Lett.* **13**, 38 (2021). <https://doi.org/10.1007/s40820-020-00558-3>
10. P.K. Kannan, D.J. Late, H. Morgan, C.S. Rout, Recent developments in 2D layered inorganic nanomaterials for sensing. *Nanoscale* **7**, 13293–13312 (2015). <https://doi.org/10.1039/C5NR03633J>
11. R. Kumar, W. Zheng, X. Liu, J. Zhang, M. Kumar, MoS₂-based nanomaterials for room-temperature gas sensors. *Adv. Mater. Technol.* **5**, 1901062 (2020). <https://doi.org/10.1002/admt.201901062>
12. D. Zhang, J. Wu, P. Li, Y. Cao, Room-temperature SO₂ gas-sensing properties based on a metal-doped MoS₂ nanoflower: an experimental and density functional theory investigation. *J. Mater. Chem. A* **5**, 20666–20677 (2017). <https://doi.org/10.1039/C7TA07001B>
13. Z. Xue, M. Yan, X. Wang, Z. Wang, Y. Zhang et al., Tailoring unsymmetrical-coordinated atomic site in oxide-supported Pt catalysts for enhanced surface activity and stability. *Small* **17**, e2101008 (2021). <https://doi.org/10.1002/smll.202101008>
14. L. Liu, P. Zhou, X. Su, Y. Liu, Y. Sun et al., Synergistic Ni single atoms and oxygen vacancies on SnO₂ nanorods toward promoting SO₂ gas sensing. *Sens. Actuat. B Chem.* **351**, 130983 (2022). <https://doi.org/10.1016/j.snb.2021.130983>
15. Z. Li, E. Tian, S. Wang, M. Ye, S. Li et al., Single-atom catalysts: promoters of highly sensitive and selective sensors. *Chem. Soc. Rev.* **52**, 5088–5134 (2023). <https://doi.org/10.1039/d2cs00191h>
16. M. Yan, X. Gao, X. Han, D. Zhou, Y. Lin et al., Harvesting the gas molecules by bioinspired design of 1D/2D hybrids toward sensitive acetone detecting. *Small Struct.* **4**, 2200248 (2023). <https://doi.org/10.1002/sstr.202200248>
17. Z. Xue, M. Yan, X. Yu, Y. Tong, H. Zhou et al., One-dimensional segregated single Au sites on step-rich ZnO ladder for ultrasensitive NO₂ sensors. *Chem* **6**, 3364–3373 (2020). <https://doi.org/10.1016/j.chempr.2020.09.026>
18. N. Luo, H. Cai, B. Lu, Z. Xue, J. Xu, Pt-functionalized amorphous RuO_x as excellent stability and high-activity catalysts for low temperature MEMS sensors. *Small* **19**, e2300006 (2023). <https://doi.org/10.1002/smll.202300006>
19. H. Cai, N. Luo, X. Wang, M. Guo, X. Li et al., Kinetics-driven dual hydrogen spillover effects for ultrasensitive hydrogen sensing. *Small* **19**, e2302652 (2023). <https://doi.org/10.1002/smll.202302652>
20. W.-T. Koo, Y. Kim, S. Kim, B.L. Suh, S. Savagatrup et al., Hydrogen sensors from composites of ultra-small bimetallic nanoparticles and porous ion-exchange polymers. *Chem* **6**, 2746–2758 (2020). <https://doi.org/10.1016/j.chempr.2020.07.015>
21. H. Zhang, X.F. Lu, Z.-P. Wu, X.W.D. Lou, Emerging multifunctional single-atom catalysts/nanozymes. *ACS Cent. Sci.* **6**, 1288 (2020). <https://doi.org/10.1021/acscentsci.0c00512>
22. Y. Guo, M. Wang, Q. Zhu, D. Xiao, D. Ma, Ensemble effect for single-atom, small cluster and nanoparticle catalysts. *Nat. Catal.* **5**, 766–776 (2022). <https://doi.org/10.1038/s41929-022-00839-7>
23. H. Shin, W.-G. Jung, D.-H. Kim, J.-S. Jang, Y.H. Kim et al., Single-atom Pt stabilized on one-dimensional nanostructure support via carbon nitride/SnO₂ heterojunction trapping. *ACS Nano* **14**, 11394 (2020). <https://doi.org/10.1021/acsnano.0c03687>
24. J. Qiu, X. Hu, L. Shi, J. Fan, X. Min et al., Enabling selective, room-temperature gas detection using atomically dispersed Zn. *Sens. Actuators B Chem.* **329**, 129221 (2021). <https://doi.org/10.1016/j.snb.2020.129221>
25. F. Gu, Y. Cui, D. Han, S. Hong, M. Flytzani-Stephanopoulos et al., Atomically dispersed Pt(II) on WO₃ for highly selective sensing and catalytic oxidation of triethylamine. *Appl. Catal. B Environ.* **256**, 117809 (2019). <https://doi.org/10.1016/j.apcatb.2019.117809>
26. Z. Xue, C. Wang, Y. Tong, M. Yan, J. Zhang et al., Strain-assisted single Pt sites on high-curvature MoS₂ surface for ultrasensitive H₂S sensing. *CCS Chem.* **4**, 3842 (2022)
27. Z. Pei, H. Zhang, Z.-P. Wu, X.F. Lu, D. Luan et al., Atomically dispersed Ni activates adjacent Ce sites for enhanced electrocatalytic oxygen evolution activity. *Sci. Adv.* **9**, eadh1320 (2023). <https://doi.org/10.1126/sciadv.adh1320>
28. S. Zhuo, Y. Xu, W. Zhao, J. Zhang, B. Zhang, Hierarchical nanosheet-based MoS₂ nanotubes fabricated by an anion-exchange reaction of MoO₃-amine hybrid nanowires. *Angew. Chem. Int. Ed.* **52**, 8602 (2013). <https://doi.org/10.1002/anie.201303480>
29. X. Bai, X. Wang, T. Jia, L. Guo, D. Hao et al., Efficient degradation of PPCPs by Mo_{1-x}S_{2-y} with S vacancy at phase-junction: promoted by innergenerate-H₂O₂. *Appl. Catal. B Environ.* **310**, 121302 (2022). <https://doi.org/10.1016/j.apcatb.2022.121302>

30. S. Liu, Y. Yin, M. Wu, K.S. Hui, K.N. Hui et al., Phosphorus-mediated MoS₂ nanowires as a high-performance electrode material for quasi-solid-state sodium-ion intercalation supercapacitors. *Small* **15**, 1803984 (2019). <https://doi.org/10.1002/sml.201803984>
31. H. Xu, J. Li, P. Li, J. Shi, X. Gao et al., Highly efficient SO₂ sensing by light-assisted Ag/PANI/SnO₂ at room temperature and the sensing mechanism. *ACS Appl. Mater. Interfaces* **13**, 49194 (2021). <https://doi.org/10.1021/acsmi.1c14548>
32. D. Kim, S. Chong, C. Park, J. Ahn, J. Jang et al., Oxide/ZIF-8 hybrid nanofiber yarns: heightened surface activity for exceptional chemiresistive sensing. *Adv. Mater.* **34**, 2105869 (2022). <https://doi.org/10.1002/adma.202105869>
33. Z. Shen, M. Cao, Y. Wen, J. Li, X. Zhang et al., Tuning the local coordination of CoP_{1-x}S_x between NiAs- and MnP-type structures to catalyze lithium-sulfur batteries. *ACS Nano* **17**, 3143 (2023). <https://doi.org/10.1021/acsnano.2c12436>
34. Y. Men, X. Su, P. Li, Y. Tan, C. Ge et al., Oxygen-inserted top-surface layers of Ni for boosting alkaline hydrogen oxidation electrocatalysis. *J. Am. Chem. Soc.* **144**, 12661 (2022). <https://doi.org/10.1021/jacs.2c01448>
35. K. Chen, R. Dronskowski, First-principles study of divalent 3d transition-metal carbodiimides. *J. Phys. Chem. A* **123**, 9328 (2019). <https://doi.org/10.1021/acs.jpca.9b05799>
36. Z.-G. Li, X.-E. Li, H.-Y. Chen, Sulfur dioxide: an emerging signaling molecule in plants. *Front. Plant Sci.* **13**, 891626 (2022). <https://doi.org/10.3389/fpls.2022.891626>
37. H. Yin, Y. Cao, B. Marelli, X. Zeng, A.J. Mason et al., Soil sensors and plant wearables for smart and precision agriculture. *Adv. Mater.* **33**, 2007764 (2021). <https://doi.org/10.1002/adma.202007764>
38. Z. Li, Y. Liu, O. Hossain, R. Paul, S. Yao et al., Real-time monitoring of plant stresses via chemiresistive profiling of leaf volatiles by a wearable sensor. *Matter* **4**, 2553 (2021). <https://doi.org/10.1016/j.matt.2021.06.009>

